Materials Science and Engineering B 269 (2021) 115167

Contents lists available at ScienceDirect

Materials Science & Engineering B

journal homepage: www.elsevier.com/locate/mseb

Synthesis and characterization of ZrO_2/CeO_2 nanocomposites for efficient removal of Acid Green 1 dye from aqueous solution

Ayman A. Ali [a,*], Sayed A. Shama [a], Alaa S. Amin [a], Sahar R. EL-Sayed [a]

[a] Chemistry Department, Faculty of Science, Benha University, Benha City, Egypt

ARTICLE INFO

Keywords:
Coprecipitation method
Combustion-ultrasonication method
ZrO_2/CeO_2 nanocomposites
Adsorption
Acid Green 1

ABSTRACT

ZrO_2/CeO_2 nanocomposites were prepared using the co-precipitation (ZCP11, ZCP12 and ZCP21 samples) and hybrid combustion-ultrasonication (ZC11, ZC12 and ZC21 samples) methods, following by the calcination. The characterization of the synthesized ZrO_2/CeO_2 nanocomposites was achieved by utilizing several analytical techniques such as High-resolution transmission electron microscopy, X-ray diffraction, Fourier transforms infrared spectra, BET method and Field emission scanning electron microscopy. The optimum conditions were evaluated from the batch method: pH = 3, 250 mg/L of AG1 dye, 0.05 g dose adsorbents, and equilibrium time (90–200 min according to the sample). The adsorption isotherm, kinetic and mechanism models analyzed using the extracted experimental data for the elimination of Acid Green 1 dye over ZCP11 and ZC11 samples. Besides, the thermodynamic factors were investigated at 293–303 K. The optimum conditions were employed for the fabricated ZrO_2/CeO_2 nanocomposite samples and the best adsorbent were reused for the elimination of AG1 dye.

1. Introduction

Dyes are colored organic compounds based on two main functional groups such as chromophoric group (NR_2, NHR, NH_2, COOH and OH), and auxochromes (N_2, NO and NO_2) [1] which lead to increasing the organic pollutants inside the water media. Dyes are widely utilized in different fields such as food processing, textile or leather manufacturing, rubber and plastics industry, paper printing, cosmetics or medicine industry [2]. Inorganic and organic pollutants have existed inside the environment area like heavy metal and dyes which considered the big problems because of their carcinogenic and toxic characteristics for living things on our planet. The trace quantity of the dye that exists in the living systems may cause several health problems to mankind as well as animals [3]. Acid Green 1 (naphthol green B) is a derivative of benzidine and naphthalic acid and metabolizes carcinogenic products. It may affect blood factors, such as induce somnolence and clotting, and respiratory problems [3]. Removing colour materials as the dyes and pigments from wastewater can be done via several methods namely chemical, biological and physical methods such as flocculation, adsorption, oxidation, electrolysis, biodegradation, ion-exchange, catalytic photodegradation, coagulation, ozonation membrane filtration, etc. Among the various available physical-chemical processes, adsorption is considered one of the most effective and confirmed methods for decolorization in water and effluent [4,5].

Inorganic nanoparticles have attracted immense interest from different fields because of their unique characteristics [6-10] such as high surface reactivity, large surface area, relatively low cost, etc. Among the various available materials, Cerium oxide (CeO2) is one of the rare earth metal oxides and it appeared in a cubic fluorite-structured (FCC). The cerium oxide structure is more stable due to its melting point and the temperature can be raised to 2700 °C [11,12]. The cerium oxide is formed the cubic structure and each cerium atom is enclosed by eight oxygen sites in FCC and each oxygen position has a tetrahedron cerium site [13,14]. Cerium oxide nanoparticles have important attention due to their unique characteristics and distinctive properties such as different size and morphology, high refractive index, high thermal stability, UV absorbing ability, facile electrical conductivity, high hardness, specific chemical reactivity, high surface area, large oxygen storage capacity, etc. According to these distinctive and unique properties, it was applied in various types of advanced applications such as gas sensor, glass polishing, free radical scavenger, catalyst, adsorbent for removal of pollutants from wastewater, the window for the semiconductor device, solar cell, elimination soot from diesel engine exhaust, ceramic material, water splitting and fuel cell [13,15,16]. The chemical formula of the

* Corresponding author.
E-mail address: ayman.abdelrazik@fsc.bu.edu.eg (A.A. Ali).

https://doi.org/10.1016/j.mseb.2021.115167
Received 19 November 2020; Received in revised form 6 March 2021; Accepted 29 March 2021
Available online 19 April 2021

zirconium oxide is ZrO_2, occasionally known as zirconia is a white crystalline oxide of zirconium [17]. ZrO_2 exhibits three important polymorphic forms: the monoclinic phase is thermodynamically stable up to 1100 °C, the tetragonal phase exists in the temperature range 1100–2370 °C, and the cubic phase is found above 2370 °C [18]. Zirconium oxide is a widely used inorganic material that is chemically stable, non-toxic, and soluble in water [19] and is of vital importance due to its thermal and chemical stability, and excellent mechanical properties, such as high strength and fracture toughness, high melting point, low thermal conductivity, and high corrosion resistance [20]. Zirconium oxide nanoparticles illustrate intriguing much attention of researchers due to their unique physical, chemical, optical, and electrical properties. It used in different applications such as sensing, catalysis, paint, coatings, wastewater treatment, fuel cells and advanced ceramics [21].

In recent years, the synthesized composites are used in various application due to the modified properties and unique characteristics. Composites consist of two or more phases as a mixture and one of the components is considered as a matrix or host. One of the obtained composites can be formed in the term of metal or nanometal or organic material. The second component in the mixture can be the same type or different to improve the properties of the obtained composites. The fabricated composites are considered modified and attractive materials for different applications such as zirconium oxide /chitosan composite as bone tissue engineering materials [22], ZrO_2/TiO_2 composites for photocatalytic degradation of organic dyes [23], Al_2O_3/ZrO_2 composite as reinforced materials [24], $ZrO_2/CeO_2/Y_2O_3$ ceramic composites with Al_2O_3 platelets for dental implants [25], Co_3O_4/ZrO_2 composites for the elimination of organic dyes [26], $Mg(OH)_2/ZrO_2$ composite for the elimination of phosphate from aqueous solution [27], CeO_2/chitosan composite for the removal of fluoride [28], CeO_2/activated carbon composite for removal of tetrachloride, chloroform and dichloromethane from water [29], CeO_2/graphene quantum dots composite for the photocatalytic degradation of rhodamine B [30], Manganese/cerium oxide composite supporting palladium nanoscale for the oxidation of toluene [31], CeO_2 doped ZnO/reduced graphene oxide composite as antibacterial material [32], etc.

Simple and nanocomposite metal oxide nano-adsorbents synthesized by utilizing multi-methods like hydrothermal synthesis [33,34], combustion synthesis [35-38], sol-gel process [39-41], co-precipitation [42-45], etc. Our work shows that the CeO_2/ZrO_2 nanocomposites were synthesized by using co-precipitation and combustion- ultrasonication methods. The obtained CeO_2/ZrO_2 nanocomposites were characterized by different techniques. The obtained CeO_2/ZrO_2 nanocomposites were used as adsorbents for the elimination of Acid Green 1 dye (AG1) from aqueous media. The kinetics, thermodynamic and isotherm of the adsorption of Acid Green 1 dye (AG1) over the synthesized nanocomposites were studied.

2. Experimental

2.1. Materials and reagents

Zirconium oxychloride octahydrate ($ZrOCl_2{\cdot}8H_2O$, 99.5%), cerium sulphate tetrahydrate ($Ce(SO_4)_2{\cdot}4H_2O$, 98.5%) and Acid Green 1 (naphthol green B: $C_{30}H_{15}FeN_3Na_3O_{15}S_3$, 99%) were obtained from Sigma–Aldrich Chemical Company. Ammonium hydroxide (NH_4OH, 33%), nitric acid (HNO_3, 69%) and Glycine ($C_2H_5NO_2$, 99%) were obtained from El Nasr pharmaceutical chemical company. The used materials (chemicals and reagents) in the experimental part were of analytical grade and used as obtained without any treatment. Freshly bidistilled water was used through all experiments. The chemical structure of Acid Green 1 is shown in Fig. 1.

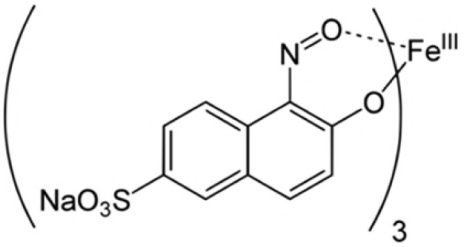

Fig. 1. The chemical structure of Acid Green 1 (AG1).

2.2. Synthesis of ZrO_2/CeO_2 nanocomposites via co-precipitation method

CeO_2/ZrO_2 as mixed oxide nanocomposites were prepared by dissolved certain amounts of zirconium oxychloride octahydrate and cerium sulphate tetrahydrate with different molar ratios (Zr/Ce = 1:1, 1:2 and 2:1) in bidistilled water. The pH of obtained solutions was controlled by ammonia solution until the precipitate appeared at pH = 9. The obtained precipitates were washed sundry times and the fabricated precipitates were standing for 2 h. The as-synthesized precipitates were dried at 150 °C overnight (24 h). The crystalline CeO_2/ZrO_2 nanocomposites were fabricated after the calcination of the dried samples at 400 °C and 500 °C for 2 h and 1 h, respectively. The schematic flowchart for the synthesized of the ZrO_2/CeO_2 using the co-precipitation method is shown in Fig. 2. The names of zirconium and cerium oxide nanocomposites are labelled according to the compositions of the starting materials as the following: (Zr/Ce (sample name) = 1:1 (ZCP11), 1:2 (ZCP12) and 2:1 (ZCP21)).

2.3. Fabrication of CeO_2/ZrO_2 nanocomposites via combustion-ultrasonication method

0.01 mol of zirconium oxychloride octahydrate was dissolved in 20 mL distilled water and precipitated by ammonia solution until pH = 9. The as-prepared white precipitate was washed several times and the estimated amount of nitric acid (HNO_3, 2 M) was added to the obtained precipitate with stirring for 2 h to obtain zirconium oxynitrate. The obtained solution was mixed with the determined moles of glycine fuel according to the rules of the combustion technique and Eq. No. 1. The solution was heated on a hot plate at 120 °C until the viscous gel was produced. The obtained gel was ignited at 250 °C for a few minutes, a pale-grey powder was prepared. The as-prepared powder was calcined at 500 °C for 2 h, following by the calcination at 700 °C for 15 min to get the pure white and crystalline zirconium oxide nanoparticles (ZrO_2: ZG). 0.01 mol of cerium sulphate tetrahydrate was dissolved in 20 mL bidistilled water. The pH of the obtained solution controlled by ammonia solution until the precipitate appeared at pH = 9. The obtained precipitate was washed several times and a certain amount of nitric acid was added to the obtained precipitate with stirring at 80 °C for 2 h. After the clear solution appeared, the calculated amount of glycine fuel was added according to the rules of the combustion technique and Eq. No. 2. The solution heated up to 100 °C to produce the gel, following by the auto-ignition at 250 °C for a few minutes. The fabricated pale-yellow ash collected. The fabricated powder was calcined at 500 °C for 2 h to get the fine crystalline cerium oxide powder (CeO_2: CG).

$$9ZrO(NO_3)_2 + 10C_2H_5NO_2 \rightarrow 9ZrO_2 + 25H_2O + 20CO_2 + 14N_2 \quad (1)$$

$$9Ce(NO_3)_4 + 20C_2H_5NO_2 \rightarrow 9CeO_2 + 50H_2O + 40CO_2 + 28N_2 \quad (2)$$

Cerium and zirconium oxide nanocomposites were synthesized by mixing certain amounts of the fabricated zirconium and cerium oxides in bidistilled water (50 mL) with stirring for 5 min. The obtained mixtures ultrasonicated for 15 min followed by constant stirring for 30 min. Finally, the synthesized samples were dried in an electric oven at 100 °C for 1 h and calcined at 500 °C for 10 min. A schematic flowchart of the

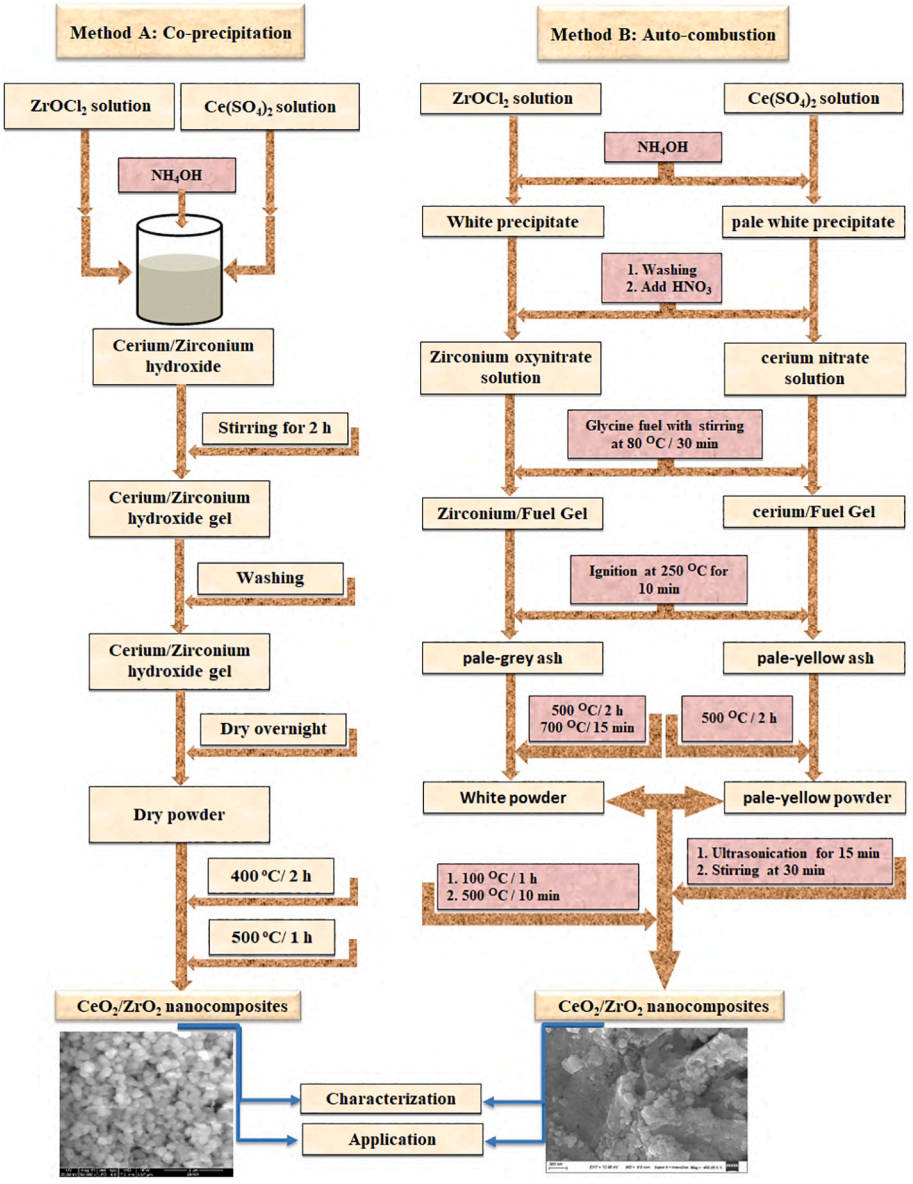

Fig. 2. Schematic flowchart for the fabrication of the ZrO_2/CeO_2 nanocomposites.

synthetic procedure for the ZrO_2/CeO_2 is shown in Fig. 2. The samples of the ZrO_2/CeO_2 nanocomposites are named according to the percentage of starting materials oxides (ZG and CG samples) as the following: ZG:CG (sample name) = 1:1 (ZC11), 1:2 (ZC12) and 2:1 (ZC21).

2.4. Characterization

The appeared phases were confirmed by recording the lines of XRD pattern for the as-prepared and annealed samples, 18 KW diffractometer (Bruker; model D 8 advance) with monochromatic Cu-Ka radiation, 1.54178 (A^o) in the angular range of 10-70° with step size 0.02° (2θ) and scan step time 0.4 (s). The as-synthesized and annealed products were recorded using the FTIR spectrometer (Thermo Scientific; model Nicolet iS10) from 4000 to 400 cm^{-1}. The morphology of the obtained product was tested utilizing field emission scanning electron microscopy (FESEM, JEOL JSM-6390). The (FE-SEM) and gold coating process by utilizing EMITECH K550X sputter coater. The morphology and particle size of the obtained samples were revealed using HR-TEM (model Tecnai G20, FEI, Netherland) at an electron voltage of 200 kV. The elimination of the testing dye was tested utilizing a Jasco UV-Vis spectrophotometer (Jasco; model V 670). The as-synthesized cerium and zirconium oxide nanocomposites (ZC11, ZG, CG and ZCP11 samples) investigated utilizing the thermal tool (TGA, DTA and DTG) from 25 °C to 600-800 °C. The TGA and DTA tests investigated with the air gas atmosphere (the heating rate = 10 °C/min) utilizing a thermal analyzer Shimadzu instrument (model TA-60WS). The surface properties of the fabricated composites samples were investigated from nitrogen adsorption isotherms at 77 K using the Brunauer Emmett Teller method (NOVAtouch model).

3. Result and discussion

3.1. Thermal analysis

Fig. 3(a-d) displays the TGA, DTG and DTA of CG, ZG, ZC11 and ZCP11 samples. The thermal recording of the as-prepared cerium oxide (CG sample) using glycine and combustion method as displayed in Fig. 3 (a). TGA curve appeared the degradation of CG sample in two steps and the total weight loss percentage estimated to be 6%. The first step occurs in between 30 and 200 °C and the weight loss percentage was estimated

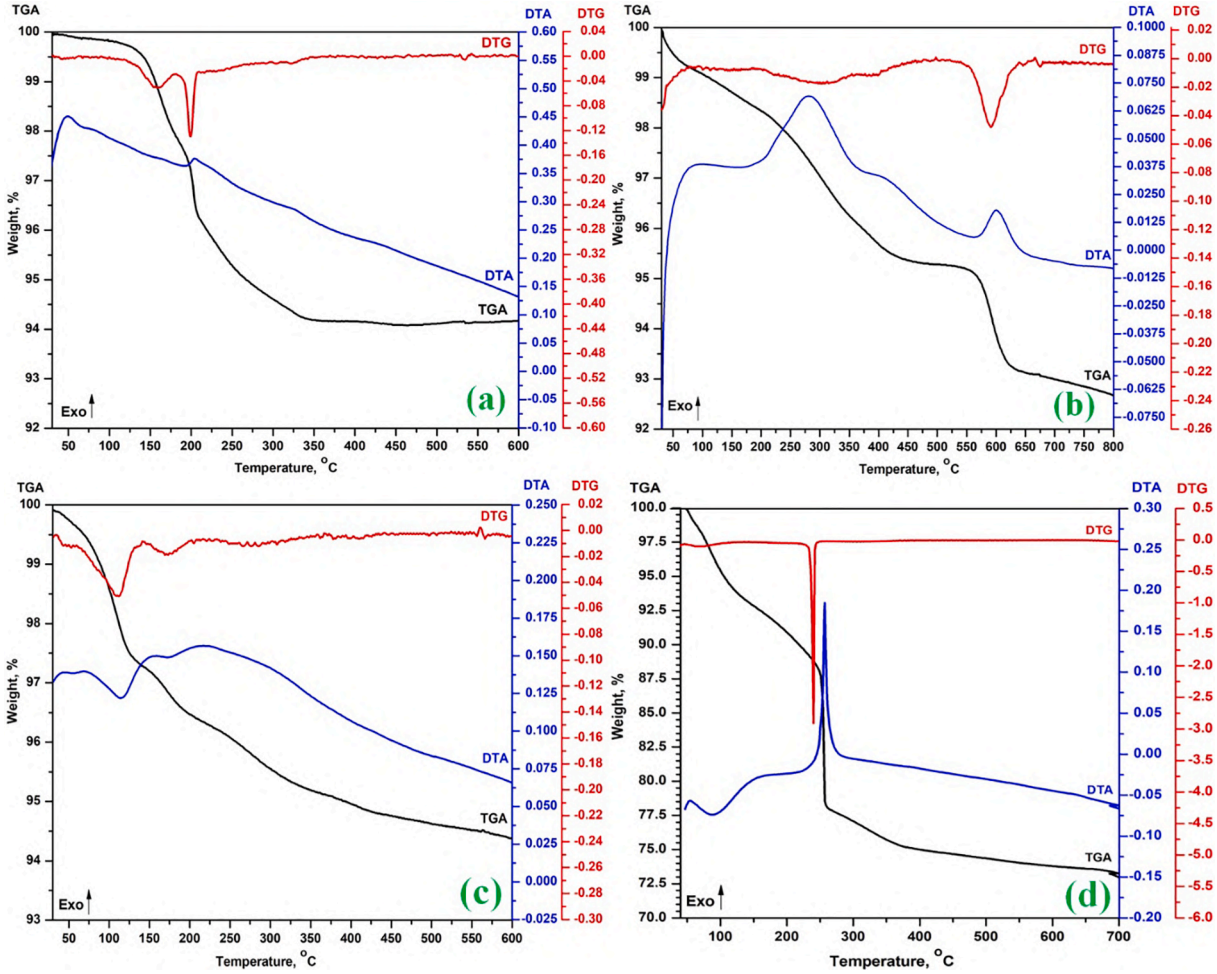

Fig. 3. Thermal analyses (TGA, DTA and DTG) of (a) CG, (b) ZG, (c) ZC11 sample and (d) ZCP11 samples.

to be 3% due to the evolution of the adsorption of water molecules and any volatile compounds on the surface of the CG sample. The second one recorded in between 200 and 450 °C (weight loss = 3%) according to the elimination of the obtained carbon and volatile organic materials after the combustion with glycine fuel. The DTG curve appeared two peaks at 155 °C and 200 °C and it confirms the extracted information from the TG curve of the CG sample. DTA curve shows the endothermic peak at 70 °C according to the elimination of the volatile materials from the CG sample. The second one is the exothermic peak at 205 °C according to the ignition of residual of the cerium nitrate with glycine in the CG sample. Form these data, the cerium oxide synthesized after the calcination of the as-prepared CG sample in between 450 and 500 °C. The thermal recording of the as-prepared zirconium oxide (ZG sample) using glycine and combustion method as displayed in Fig. 3(b). TGA curve appeared the degradation of the ZG sample in three steps (30–200 °C, 200–500 °C and 500–700 °C) and the total weight loss percentage estimated to be 7%. The weight loss percentage of the first step was estimated to be 1.5% according to the elimination of the adsorption of volatile compounds on the surface of the ZG sample. The weight losses percentage of the second and third steps displays the elimination of 3.25% and 2.25% from the sample, respectively, according to the elimination of the obtained volatile organic materials after the combustion process. The DTG curve appeared three peaks at 40 °C, 300 °C and 590 °C and it approved that the achieved information from the TG curve of the ZG sample. DTA curve shows the endothermic peaks at 40 °C according to the elimination of the volatile materials from the CG sample. The second peak is the exothermic peak at 280 °C according to the ignition of residual of the zirconium nitrate with glycine in the ZG sample. The third peak is the exothermic peak at 600 °C according to the elimination of the obtained residual from the ignition process in the ZG sample. According to these data, the zirconium oxide fabricated after the calcination of the as-prepared CG sample in between 700 and 800 °C.

The thermal analysis of the obtained zirconium and cerium oxide nanocomposite (ZC11 sample) after the mixing as displayed in Fig. 3(c). TGA curve appeared the degradation of CG sample in two steps (30–125 °C, 125–200 °C and 200–550 °C) and the total weight loss percentage estimated to be 5.5%. The weight losses percentage of the first and the second steps were estimated to be 2.5% and 1%, respectively, according to the evolution of the adsorption of the volatile compounds (eg. water molecules) on the surface of the ZC11 sample. The weight loss of the third step estimated to be 2% due to the elimination of the volatile organic materials and the recombination of the hydroxide groups on the surface of the ZC11 nanocomposite. The DTG curve appeared three peaks at 110 °C, 175 °C and 275 °C and it matched with the information of the TG curve of the ZC11 sample. DTA curve shows the two endothermic peaks at 110 °C and 175 °C due to the elimination of the volatile materials from the ZC11 sample. The third one is the exothermic peak at 220 °C according to the evolution of the residual of the recombination of the hydroxide groups and organic materials on the surface of cerium zirconium oxide nanocomposite in the ZC11 sample. Form these data, the ZC11 composite synthesized after the calcination of the as-fabricated ZC11 sample in between 500 and 600 °C. Fig. 3(d) displays the thermal analysis of the as-synthesized ZrO_2/CeO_2 nanocomposites using the co-precipitation method (ZCP11 sample). TGA curve displayed that the degradation happens in two steps and the total weight loss percentage was found to be 24.38% in the

temperature range of 30–500 °C. The first degradation step (30–175 °C) correlated to the elimination of the physical adsorbed of the volatile molecules (eg. water molecules). The weight loss percentage of the first step was found to be 8.5%. The second degradation step occurred in the range of 175–550 °C and the weight loss is equal to 17.5%. It explains that the degradation of the hydroxide groups from the ZCP11 sample and the gases evolved. DTG curve showed two peaks at 83 °C and 242 °C and it matched with the TGA curve. DTA curve showed one endothermic peak at 90 °C related to the elimination of volatile molecules. Besides, the observed exothermic band in the DTA curve at 258 °C is ascribed to the degradation of the hydroxide groups and the evolution of the gases from the ZCP11 sample. From the thermal analysis, ZrO_2/CeO_2 nanocomposites (ZCP11 sample) were fabricated after the calcination in between 400 and 550 °C.

3.2. X-ray studies

Fig. 4a(i and ii) manifests the XRD lines of the obtained ZrO_2/CeO_2 nanocomposites with different molar ratios (1:1, 1:2 and 2:1) using auto-combustion and coprecipitation methods. The XRD lines of the obtained ZrO_2/CeO_2 nanocomposites using the combustion-ultrasonication method (ZC11, ZC12 and ZC21 samples) manifested in Fig. 4a(i) after calcination at 500 °C for 10 min. The calcined ZrO_2/CeO_2 nanocomposites (ZC11, ZC12 and ZC21 samples) are indexed according to reference card No. 01–079-1796 for the zirconium oxide (Crystal system: Orthorhombic; a = 5.0680 A°, b = 5.2600 A° and c = 5.0770 A° and α = β = γ = 90°) and reference card No. 01–075-0120 for the CeO_2 (Crystal system: Cubic; a = b = c = 5.4110 A° and α = β = γ = 90°). The XRD lines of the obtained ZrO_2/CeO_2 nanocomposites using the co-precipitation method (ZCP11, ZCP12 and ZCP21 samples) are manifested in Fig. 4a(ii) after calcination at 400 °C for 2 h. The calcined ZrO_2/CeO_2 samples are indexed according to reference card No. 01–078-

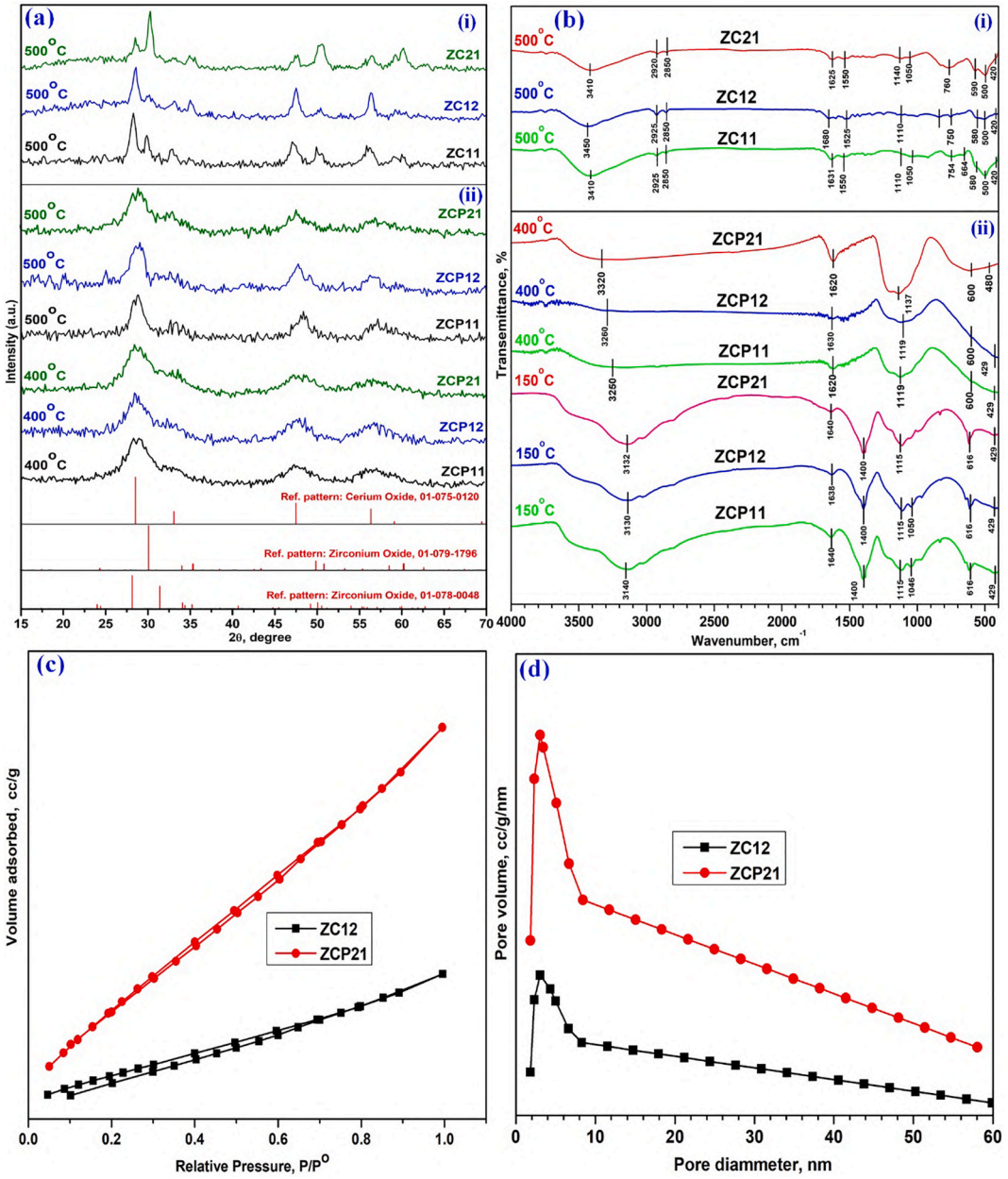

Fig. 4. XRD patterns (a), FTIR analysis (b), N_2 adsorption/desorption isotherms (c) and pore size distribution (d) of the synthesized zirconium and cerium oxide nanocomposites.

0048 for the zirconium oxide (Crystal system: Monoclinic; a = 5.1505 A°, b = 5.2031 A° and c = 5.3154 A°; α = γ = 90° and β = 99.194°) and reference card No. 01–075-0120 for the CeO_2. After the calcination at 500 °C, the intensity of XRD peaks of the ZCP11, ZCP12 and ZCP21 samples increases with the formation of cerium and zirconium oxide nanocomposites. The average crystal sizes (S, nm) of ZrO_2/CeO_2 nanocomposites (ZCP11, ZCP12, ZCP21, ZC11, ZC12 and ZC21 samples) estimated by utilizing the Debye-Scherrer formula: ($S = 0.9\lambda/\beta \cos\theta$) [9,46]. The crystallite sizes of ZrO_2/CeO_2 nanocomposites evaluated as the following: 3.25, 3.3 and 3 nm for ZCP11, ZCP12 and ZCP21 samples, respectively after the calcination at 400 °C. Besides, the crystallite sizes of ZCP11, ZCP12, ZCP21, ZC11, ZC12 and ZC21 samples were estimated to be 5, 11, 5, 15, 11, 12 nm, respectively after the calcination at 500 °C. According to the XRD data, the stable ZrO_2/CeO_2 nanocomposites are formed between 400 and 500 °C and sizes of all samples were found in the nanosized (5–15 nm). It reflected the elimination of AG1 dye on the obtained nanocomposites (ZCP11, ZCP12, ZCP21, ZC11, ZC12 1 and ZC21 samples) without releasing any other contaminations in water from the used adsorbents. Also, it explains that the high surface area of the fabricated nanocomposites (ZCP11, ZCP12, ZCP21, ZC11, ZC12 1 and ZC21 samples) according to the small sizes and reflects the removal capacity values of the AG1 dye on the prepared nanocomposites.

3.3. FTIR spectrum

Fig. 4b(i and ii) show FTIR spectra of ZrO_2/CeO_2 samples using auto-combustion and co-precipitation methods. Fig. 4b(i) displays the FTIR spectra of ZrO_2/CeO_2 nanocomposites (ZC11, ZC12 and ZC21 samples) utilizing the auto-combustion method after the calcination at 500 °C. The weak absorption bands at 3410–3450 cm^{-1}, 1625–1680 cm^{-1}, 1050–1140 cm^{-1}, 1525–1550 cm^{-1} and 2850–2925 cm^{-1} for obtained ZrO_2/CeO_2 nanocomposites (ZC11, ZC12 and ZC21 samples) are harmonized to the vibration modes of the stretching and bending vibration of hydroxyl groups, Ce-O-Ce, C-O and CH aliphatic, respectively. The strong absorption bands in the range 400–800 cm^{-1} (420 cm^{-1}, 500 cm^{-1}, 580–590 cm^{-1}, 664 cm^{-1}, 750–760 cm^{-1}) are corresponding to the stretching and bending vibration mode of Zr-O and Ce-O inside the ZrO_2/CeO_2 nanocomposites. Fig. 4b(ii) shows FTIR spectra of ZrO_2/CeO_2 nanocomposites (ZCP11, ZCP12 and ZCP21 samples) utilizing the co-precipitation method after the drying and calcination at 150 °C and 500 °C, respectively. After the drying at 150 °C for the ZCP11, ZCP12, ZCP21 samples. The bands at 3000–3600 cm^{-1}, 1638–1640 cm^{-1}, 1400 cm^{-1}, 1046–1115 cm^{-1} and 400–800 cm^{-1} are harmonized to vibrational modes of the stretching and bending of –OH, C=O, Ce-O-Ce and Zr-O/Ce-O groups, respectively. After the calcination at 400 °C, the weak absorption bands at 3220–3320 cm^{-1}, 1620–1630 cm^{-1}, 1119–1137 cm^{-1} for all obtained samples are corresponding to the vibration modes of stretching and bending vibration for –OH, Ce-O-Ce, respectively. The strong absorption peaks in the range 400–800 cm^{-1} (429–480 cm^{-1} and 600 cm^{-1}) for ZCP11, ZCP12 and ZCP21 samples are harmonized to the Zr-O and Ce-O stretching vibration mode of ZrO_2 and CeO_2 nanocomposites [40,47,48]. Due to the extracted information from FTIR spectra (400–4000 cm^{-1}), the stable ZrO_2/CeO_2 nanocomposites (ZC11, ZC12, ZC21ZCP11, ZCP12 and ZCP21 samples) are obtained. It reflected the adsorption of organic dye on the fabricated nanocomposites (ZC11, ZC12, ZC21ZCP11, ZCP12 and ZCP21 samples) without releasing any contaminations inside the media from the surface of the adsorbent. Also, it explains the activity of the surface of the synthesized nanocomposite according to the bonding of the hydroxide groups on the surface of ZrO_2/CeO_2 nanocomposites (ZC11, ZC12, ZC21ZCP11, ZCP12 and ZCP21 samples) and it reflects on the pH value of the AG1 dye elimination on the fabricated nanocomposites.

3.4. Surface properties of the synthesized nanocomposites

Adsorption-desorption isotherms of the fabricated ZrO_2/CeO_2 nanocomposites (ZC12 and ZCP21 samples) are manifested in Fig. 4(c). The shapes of isotherms and hysteresis loops used for the determination of the porous structures of the fabricated samples. The obtained isotherms for the synthesized ZC12 and ZCP21 samples are linked to type IV of Brunauer's categorization. The isotherm type appeared that the fabricated nanocomposites can be indicated to mesopores materials according to the heterogeneous feature of the solid surface. BET surface area, average pore diameter and total pore volume estimated to be 19.4 m^2/g, 1.812 nm, 0.0349 cc/g and 40 m^2/g, 1.808 nm, 0.06862 cc/g for ZC12 and ZCP21 samples, respectively. The BJH pore size distribution of ZC12 and ZCP21 samples displayed in Fig. 4(d). The data appeared the peaks in between 1 and 9 nm with the head at 3 nm and the extracted results manifested that the synthesized ZC12 and ZCP21 samples formed the mesopores according to the following classification: micropores (0 nm < pore diameter < 2 nm), mesopores (2 nm < pore diameter < 50 nm), and macropores (pore diameter > 50 nm) [49]. The relation between the shape of the hysteresis loop of a type IV isotherm and the texture of the fabricated nanocomposites samples appeared in the mesopores structure. According to extracted information from the surface analysis, values of the surface area and the total pore volume for the ZCP21 sample are more than the value for the ZC12 sample. It reflected on the application of the adsorption of AG1 dye on the ZC12 and ZCP21 samples and an extracted information appeared the removal capacity for the ZCP21 sample is greater than the ZC12 sample at the applied optimum conditions for the elimination dye.

3.5. Morphology studies

The morphology of ZrO_2 and CeO_2 nanocomposites (ZCP11 and ZC11 samples) are examined using FE-SEM and HR-TEM, as manifested in Figs. 5 and 6, respectively. FE-SEM images of the obtained ZrO_2/CeO_2 nanocomposites (ZCP11 sample) are manifested in Fig. 5(i-iii). The FE-SEM micrographs of the ZCP11 sample manifest the uniform spherical shape of zirconium and cerium oxide nanocomposites with hard agglomeration. The average grain sizes of the collected and visible spherical shape for the calcined ZCP11 sample was estimated to be 300 nm as manifested in Fig. 5(iii). FE-SEM micrographs of the synthesized ZrO_2/CeO_2 nanocomposites (ZC11 sample) are manifested in Fig. 5(iv-vi). SEM images of the ZC11 sample are consist of soft agglomerations of regular and irregular spherical zirconium/cerium oxide nanocomposites. The average grain sizes of the calcined ZC11 sample are about 250 nm. Elemental analysis of ZCP11 and ZC11 samples were examined utilizing the EDX technique as manifested in Fig. 5(vii-viii), respectively. Images appeared the four lines: Zr, Ce, C and O elements and it reflects the formation of the pure ZrO_2/CeO_2 nanocomposites for the synthesized samples. Carbon appeared according to the carbon grid of the SEM/EDX technique. Fig. 5(x) manifests the EDXS mapping of the ZC11 sample (Fig. 5(ix)). It appears that the synthesized CeO_2/ZrO_2 composite contains the cerium (yellow color), zirconium (red color) and oxygen (green color) elements with good distribution. EDXS mapping showed that the zirconium oxide homogeneously distributed inside the cerium oxide. Besides, it matched with the collected information from the EDXS pattern of the ZC11 sample for the presence of the zirconium oxide and cerium oxide as a mixture inside the composite.

HR-TEM examination of ZrO_2 and CeO_2 nanocomposites are manifested in Fig. 6(i-iii) and (vii-xi) for ZCP11 and ZC11 samples, respectively. HR-TEM images of the ZCP11 sample appeared the regular and irregular spherical shapes with hard and dense agglomerations as manifested in Fig. 6(i-iii). The collected information utilized for the construction of the histogram graph is appeared in Fig. 6(vi). From the TEM image and histogram graph of the ZCP11 sample, the average particle sizes are estimated be 24 nm (standard deviation (SD) = 7.6 and mean = 23.7). The calculated particle size differentiated from the determined crystallite size of the ZCP11 sample. The dense agglomerations of the particles of the synthesized cerium oxide and zirconium oxide composite (ZCP11 sample) appeared. HR-TEM micrographs of the

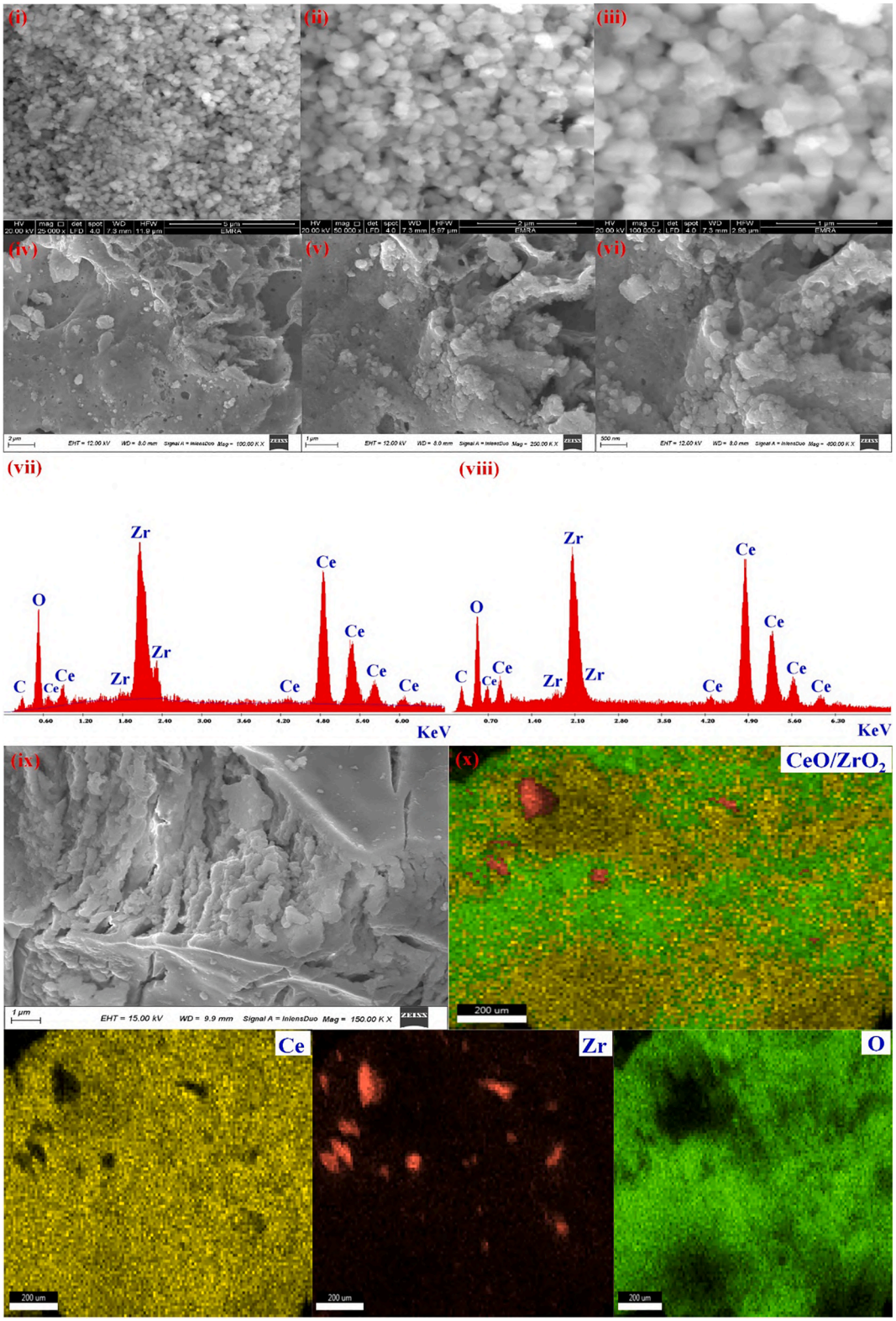

Fig. 5. FE-SEM images (i-vi) of the calcined ZrO_2/CeO_2 nanocomposite: ZCP11 (i-iii) and ZC11 (iv-vi) samples, EDX pattern of ZCP11 (vii) and ZC11 (viii) samples and the EDXS mapping (x) of ZC11 sample (ix).

calcined ZC11 sample (Fig. 6(vii-xi)) observed that the ZC11 sample consisted of the soft collection for the particles of spherical shapes with average particle sizes are about 16 nm. Also, the obtained data utilized for the construction of the histogram graph as manifested in Fig. 6(xii). From the TEM image and histogram graph of the ZC11 sample, the average particle sizes are estimated to be 16 nm (standard deviation (SD) = 7.6 and mean = 15.55). The estimated particle size differentiated from the estimated crystallite size of the ZC11 sample and the dense agglomerations of the particles of the fabricated cerium oxide and zirconium oxide composite (ZC11 sample) appeared.

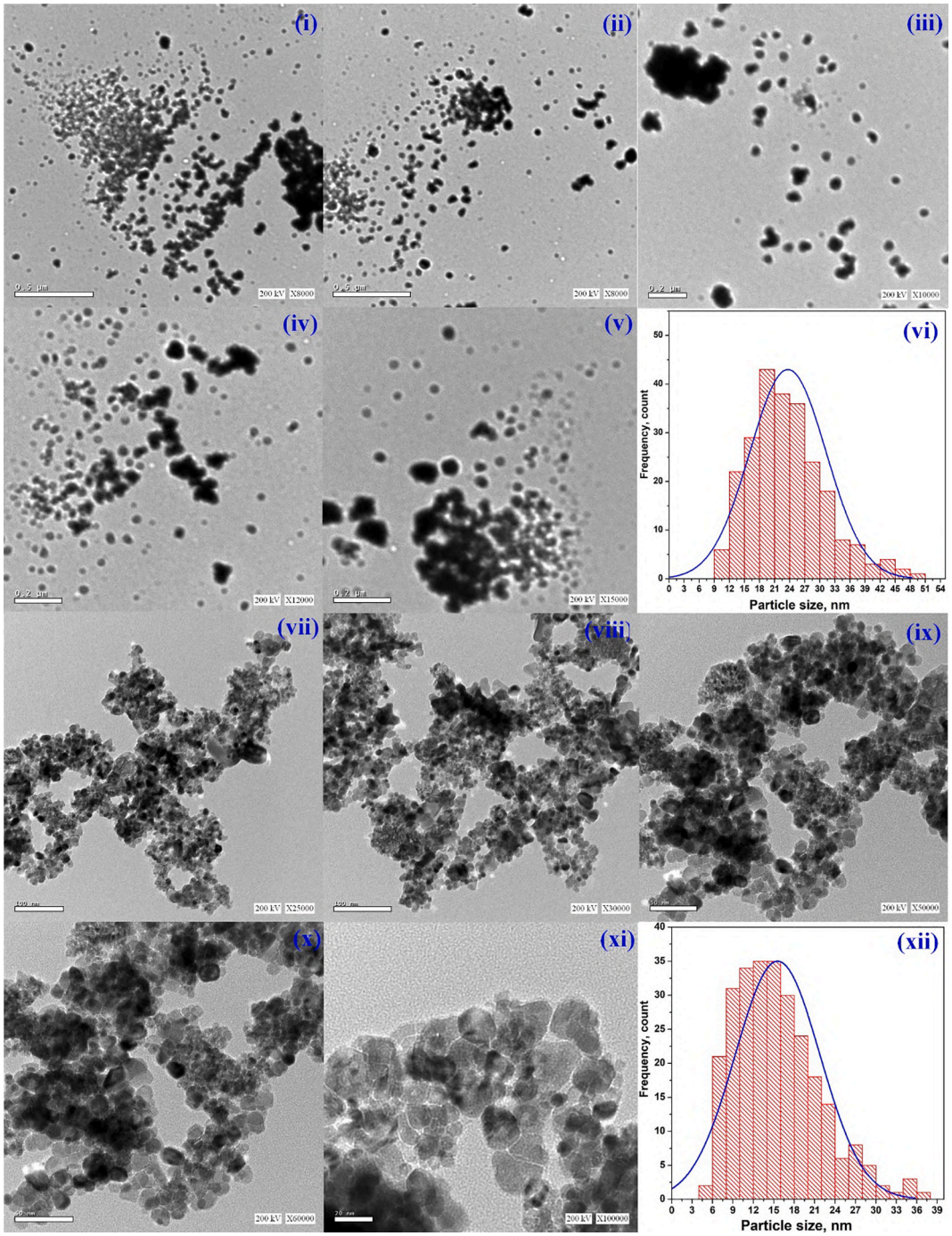

Fig. 6. HR-TEM images of the calcined ZrO_2/CeO_2 nanocomposite: ZCP11 (i-v) and ZC11 (vii-xi) samples and histogram graph for ZCP11 (vi) and ZC11 (xii) samples.

3.6. Batch adsorption experiments of Acid Green 1

The synthesized ZrO_2 and CeO_2 nanocomposites in the form of the ZCP11 and ZC11 utilized as nano-adsorbents for the separation of Acid Green 1 from aqueous solution using the batch mode. The amount of the dye adsorbed on the fabricated ZCP11 and ZC11 samples and the elimination efficiency percentage (R %) were determined from Equations No. 3 and 4, respectively.

$$q_e = \frac{(X_O - X_e)Z}{M} \tag{3}$$

$$\text{Removal}(R\%) = \frac{(X_O - X_e)}{X_O} \times 100 \tag{4}$$

Where, q_e is the amount of dye molecules adsorbed per unit weight of adsorbent (mg g^{-1}), Z is the volume of solution (L), X_o is the initial dye concentration (mg/L), X_e is the equilibrium dye concentration (mg/L), and M is the weight of the adsorbent (g).

Fig. 7(a) manifests the effect of initial pH (2 to 9) on the removal of 50 mg/L of AG 1 dye solution over 50 mg of the synthesized ZrO_2/CeO_2 nanocomposites (ZCP11 and ZC11 samples) at 293 K. The removal efficiency appeared a descending direction by the rising of the values of pH. The elimination dye efficiency recorded at λ max = 714 nm with the maximum values: 78% and 99% at pH = 3 for the elimination of AG1 dye over ZCP11 and ZC11 samples, respectively. It is expected because the surface of the synthesized nanocomposites is more protinated at low pH values. The partial positive charges are formed on the surface of the

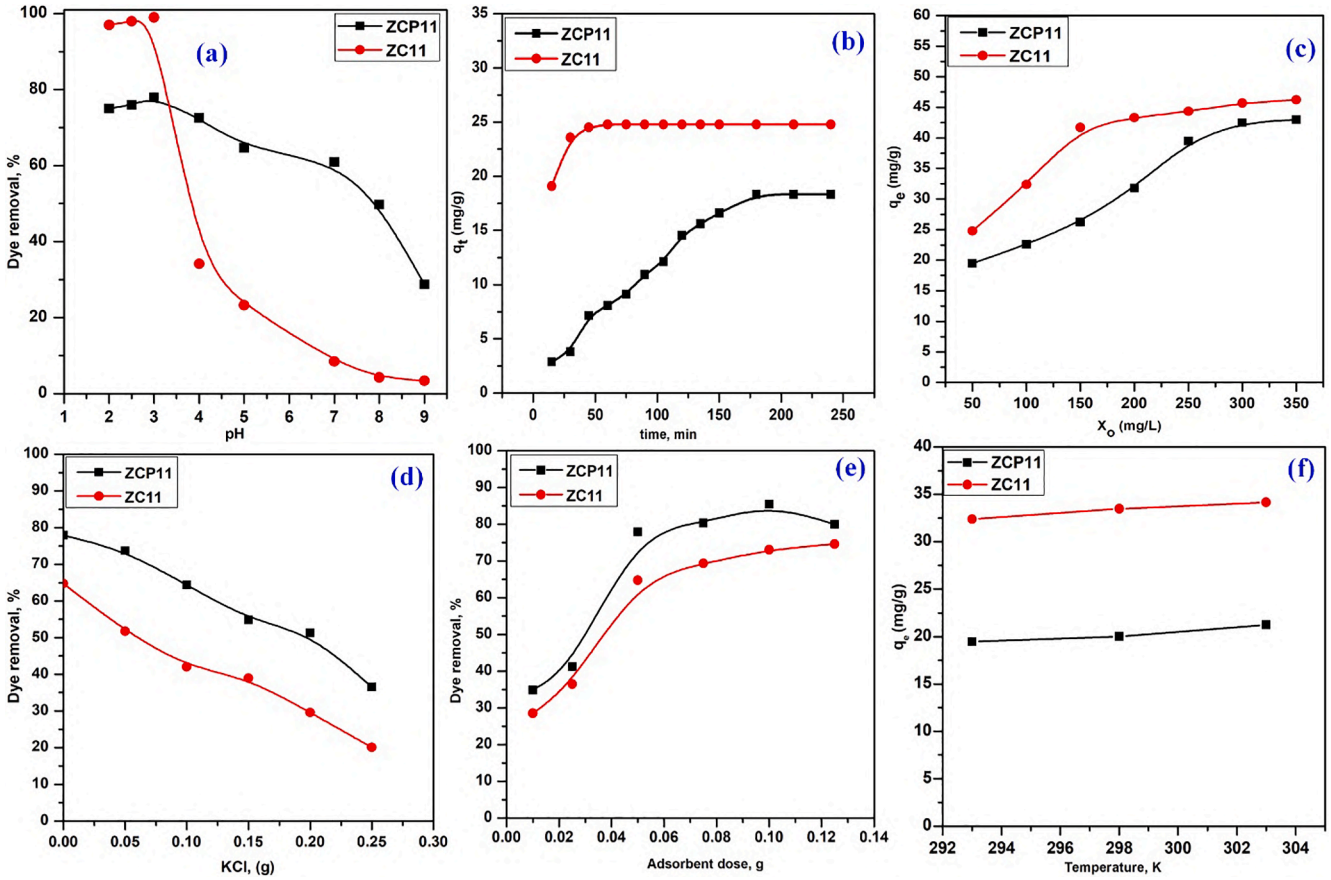

Fig. 7. Influence of pH (a), time (b), initial dye concentration (c), ionic strength (d), adsorbent dose (e), temperature (f) for the AG1 dye removal using ZrO_2/CeO_2 nanocomposite: (ZCP11 and ZC11 samples).

cerium and zirconium oxide nanocomposites and the obtained charges are enough to attract the anionic dye (Acid Green 1) from the solution. According to this data, the adsorption capacities are high in acidic media (pH = 3–5). With the increase of pH, deprotination occurs and the surface becomes more negative charge. The presence of the negative charge reduces the adsorption of the anionic dye on to the surface of the synthesized nanocomposites. According to this data, the low removal of the dye appears at high pH values [50].

The contact time of the 50 mg/L of AG1 removal was investigated using 50 mg of ZCP11 and ZC11 samples at pH 3. Fig. 7(b) shows the elimination efficiencies for the AG1 over of the synthesized ZrO_2/CeO_2 nanocomposites (ZCP11 and ZC11 samples) as a relation with the contact times from 15 min to 240 min. In the initial step, the rate of removal was fast following by the slow stage until the surface of the ZCP11 and ZC11 samples became a saturation state. The maximum removal of AG1 dye was recorded to be 19.5 mg/g and 24.8 mg/g in 200 min and 90 min for ZCP11 and ZC11 samples, respectively. Fig. 7(c) manifested the effect of various initial concentration (50 and 350 mg/L) of AG1 dye over 0.05 g of adsorbents (ZCP11 and ZC11 samples) at 293 K and pH = 3. The adsorption capacities were determined from the extracted data and equilibrium time (after 200 min and 90 min for ZCP11 and ZC11 samples, respectively). The rate of uptake was rapid in the beginning because the most active sites are free and available on the surface of the ZCP11 and ZC11 samples. The active positions on the surface of nanocomposites were blocked and closed with time, the removal rate of the dye reduced. From extracted data, the adsorption capacities of ZCP11 and ZC11 samples were determined to be 43 and 46 mg/g, respectively.

The effect of KCl on the adsorption of AG1 dye over 0.05 g of ZCP11 and ZC11 adsorbents was investigated using 0.05 to 0.25 g of KCl salt at a constant dye concentration of (50 mg/L for ZCP11 sample) and (100 mg/L for ZC11 sample) at pH = 3 and 293 K. The effect of the presence of KCl salt as ionic strength on the adsorption capability was exhibited in Fig. 7(d). From the extracted data, the dose of KCl increases, the percentage of AG1 dye elimination efficiency reduces due to the diminishing of the active positions on the surface of ZrO_2/CeO_2 nanocomposites because of the rise of the ionic strength of the solution in the presence of KCl. The effect of adsorbent dosage on the adsorption of AG1 dye was investigated using the various amounts of the adsorbent (0.01–0.125 g). The adsorbent was added to 25 mL of AG1 dye solutions of initial concentrations (50 mg/L and 100 mg/L of AG1 dye for ZCP11 and ZC11 samples, respectively). After equilibrium time, the obtained data from the adsorption of the AG1 dye over the ZCP11 and ZC11 samples are depicted in Fig. 7(e). The obtained results appeared that the increase in the amount of ZrO_2/CeO_2 adsorbent dues to the increasing in the elimination of AG1 dye efficiency due to the expanding of the active positions in the adsorbent surface. The maximum elimination percentage for the AG1 dye over 50 mg of ZCP11 and ZC11 samples were determined to be 78% and 65%, respectively.

The adsorption process was investigated with the different temperature at 293, 298 and 303 K, separately for the removal of AG1 dye (50 mg/L for ZCP11 sample) and (100 mg/L for ZC11 sample) using 0.05 g of the ZrO_2/CeO_2 nano-adsorbents. The experimental data appeared that the increase in the solution temperature leads to the increasing of the adsorption capacity slowly for the removal of AG1 dye on the ZCP11 and ZC11 samples as exhibited in Fig. 7(f). It explains that the removal of AG1 dye on the fabricated ZrO_2/CeO_2 adsorbents showed an endothermic effect. The increase in temperature of the dye solution leads to the reduction of the distance of the boundary layer around the ZCP11 and ZC11 samples. Also, the resistance from the mass transfer of adsorbate in the boundary layer around the ZrO_2/CeO_2 adsorbents

reduced with the rise of temperature and it leads to an increase in the transportability of the AG1 dye molecules [3,51].

3.7. Adsorption isotherms studies

The adsorption isotherm models were carried out by studying the relationship between the different initial concentrations of the dye (50–350 mg/L) and the adsorption capacities. Langmuir, Freundlich and Temkin isotherm models are used for the characterization of the experimental data utilizing the different equilibrium concentrations of AG1 dye (50–350 mg/L) on 50 mg of the ZCP11 and ZC11 samples at pH = 3 and 293 K as shown in Fig. 8(a-c). Linear plots of Langmuir [52-54] (Xe/qe with Xe), Freundlich [55,56] (ln qe with ln Xe) and Temkin [57] (q_e with ln Xe) isotherm models are manifested in Fig. 8(a, b and c) according to the equations No. 5, 6 and 7, respectively.

$$\frac{X_e}{q_e} = \frac{1}{K_L\, q_m} + \frac{X_e}{q_m} \tag{5}$$

$$\ln q_e = \ln K_f + \frac{1}{y} \ln X_e \tag{6}$$

$$q_e = B \ln K_T + B \ln X_e \tag{7}$$

Where, q_e is the equilibrium adsorption capacity of AG1 dye on the ZCP11 and ZC11 adsorbents, K_L is the Langmuir constant (L/mg), q_m is the maximum amount of adsorbed solute to adsorbent (mg/g). K_F is the Freundlich parameter (mg/g), (1/y) is the heterogeneity factor, B is constant (B = RT/d), K_T (L/mg) is Temkin equilibrium binding parameter related to the maximum binding energy and d corresponds to the heat of adsorption [58]. From the Langmuir isotherm, the equilibrium parameter can calculate from $R_L = 1/(1 + S)$, $S = K_L X_o$ and the R_L values show the nature of the adsorption of the dye. According to the Freundlich isotherm, the maximum adsorption capacity can calculate using the relation: $q_m = K_F X_o^{1/y}$. If the value of (1/y) < 1, it indicates normal adsorption. Also, the value of y in between 1 < y < 10, indicates a favorable adsorption process [59]. According to the Temkin isotherm, the heat of adsorption determine using (d = RT/B), where T is the temperature in kelvin and R is the universal gas constant (8.315 J mol^{-1} K^{-1}) [60].

Table 1 is summarized the calculated parameters from Langmuir,

Table 1
The extracted parameters from Langmuir, Freundlich and Temkin isotherms for ZrO_2-CeO_2 adsorbent (ZCP11 and ZC11 samples).

isotherm	Parameters	Values	
		ZCP11	ZC11
Langmuir	K_L (L/mg)	0.0204	0.1144
	$q_{m\ (cal)}$ (mg/g)	47.62	47.40
	R_L	0.1229–0.4952	0.02437–0.14885
	R^2	0.9429	0.9973
	$qm_{\ (exp)}$ (mg/g)	43	46
Freundlich	K_F [(L/mg) $(L/mg)^{1/n}$]	9.5162	26.285
	$q_{m\ (cal)}$ (mg/g)	42	46.5
	y (L/mg)	3.9017	10.2775
	R^2	0.6262	0.8992
	$q_{m\ (exp)}$ (mg/g)	43	46
Temkin	K_T (L/g)	1.634	2203.74
	d (kJ/mol)	0.309	0.713
	B	7.884	3.418
	R^2	0.7814	0.8884

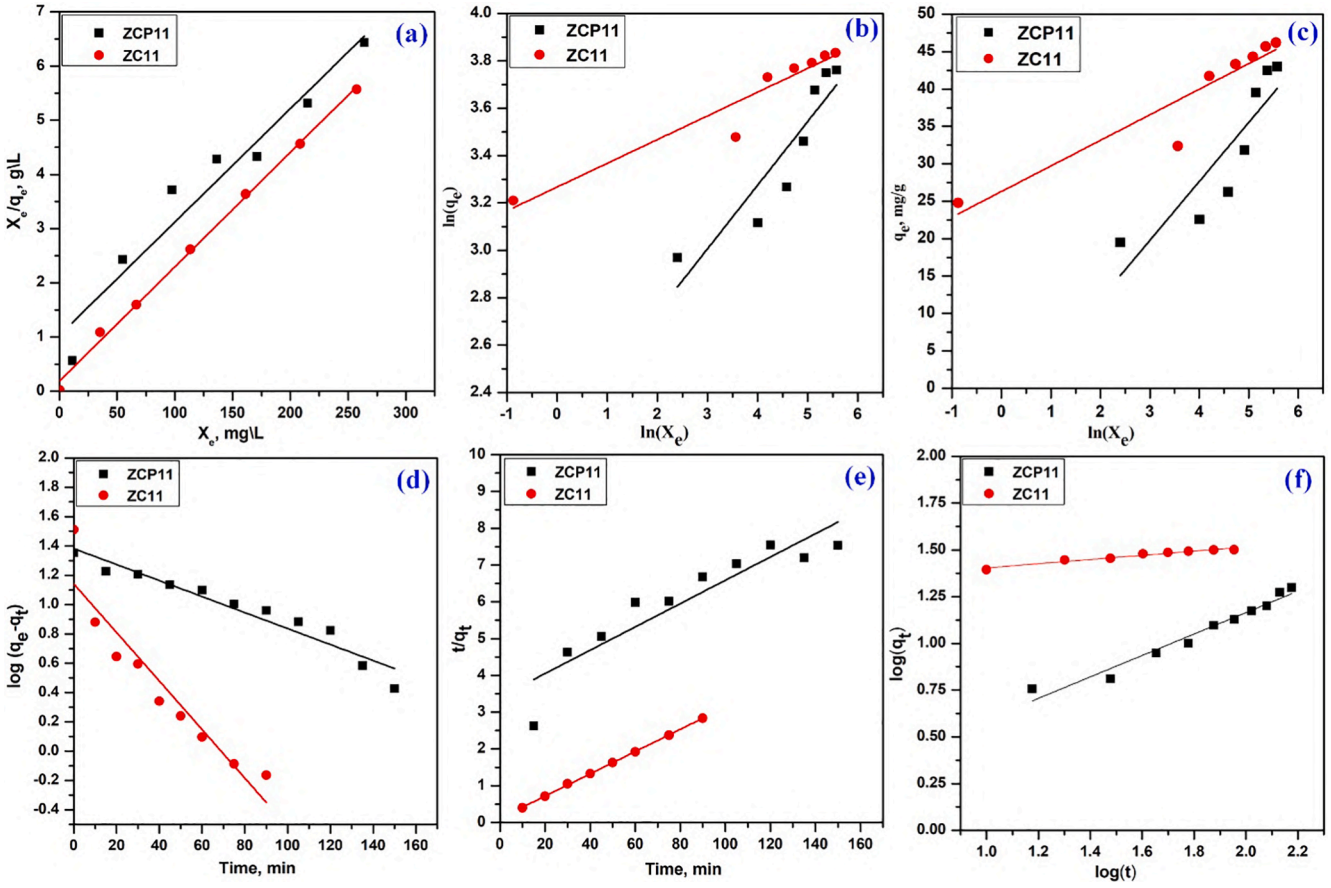

Fig. 8. Isotherm (Langmuir (a), Freundlich (b) and Temkin (c) models), pseudo-first-order model (d), pseudo-second-order model (e) and power function model (f) for the AG1 dye removal using ZrO_2/CeO_2 nanocomposite: (ZCP11 and ZC11 samples).

Freundlich and Temkin isotherms. According to the R^2 values, the model of Langmuir isotherm is the best fitting than the other isotherms. The R^2 value of the Langmuir equation was found to be 0.9429 and 0.9973 and it was closer to 1, compared to the R^2 value obtained from the other isotherms model. It explains that the removal of the AG1 dye on the fabricated ZCP11 and ZC11 adsorbents in the form of the homogenous monolayer [61]. The maximum adsorption capacity was determined to be 43 and 46 mg/g for the ZCP11 and ZC11 samples, respectively.

Also, the determined adsorption capacity from the Langmuir isotherm was calculated and found to be 47.62 and 47.4 mg/g for the synthesized ZrO_2/CeO_2 samples (ZCP11 and ZC11 adsorbents) which are closed with the experimental values (43 and 46 mg/g). In the current research, the values of the R_L parameter were calculated and found in between 0.1229 and 0.4952 and 0.02437–0.14885 for ZCP11 and ZC11 adsorbents, respectively, related to 50–300 mg/g of AG1 dye as initial concentration. It explains that the adsorption of the AG1 dye on the fabricated ZCP11 and ZC11 adsorbents is a favorable mode. From the obtained data of Freundlich isotherm, the K_F is the Freundlich constant found to be 9.5162 and 26.285 (mg/g) for ZCP11 and ZC11 adsorbents. From the obtained information of Temkin isotherm, the values of the heat of adsorption (d) were found in between 0.309 and 0.713 KJ/mole and it explains the weak interaction force between the AG1 dye and the surface of the ZCP11 and ZC11 adsorbents. Besides, the K_T found to be 1.63365 and 2203.74 L/g and the Temkin parameter (B) value calculated to be 7.884 and 3.418 J/mol for ZCP11 and ZC11 adsorbents.

3.8. Adsorption kinetic models

The models of adsorption kinetic examined by the investigation of the contact time effect on the AG1 dye removal using the prepared ZCP11 and ZC11 adsorbents. Kinetic factors of the elimination AG1 dye on ZrO_2/CeO_2 nano-adsorbent were estimated using pseudo-first-order equation (Eq. No. 8: plot log (q_e - q_t) versus t) [62], pseudo-second-order equation (Eq. No. 9: plot t/ q_t versus time t) [63] and power function kinetic equation (Eq. No. 10: plot log(q_t) versus log(t)) [64] as appeared in equations No. 8–10, respectively. The extracted information from the applied relations can get data about the rate of the AG1 dye removal using the synthesized samples as displayed in Fig. 8(d- f). The kinetic parameters determined and summarized in Table 2.

$$\log(q_e - q_t) = \log q_e - \frac{K_1 t}{2.303} \quad (8)$$

$$\frac{t}{q_t} = \frac{1}{K_2 q_e^{\,2}} + \frac{t}{q_e} \quad (9)$$

$$\log(q_t) = \log W + U\log(t) \quad (10)$$

Where, q_e and q_t are the amounts of dye adsorbed (mg/g) at equilibrium and time t (min), respectively, t (min) is contact time, and k_1 is the pseudo-first-order rate constant of adsorption (min^{-1}), k_2 (g/mg. min) is pseudo-second-order rate adsorption constant, W is the initial rate of adsorption, and U is the rate constant of the adsorption process.

According to the R^2 values From Table 2, the pseudo-first-order (ZCP11, R^2 = 0.935) is a better fitting than the pseudo-second-order (ZCP11, R^2 = 0.8529) for the elimination of the AG1 dye over ZrO_2/CeO_2 nano-adsorbent. But, the pseudo-second-order model (ZC11, R^2 = 0.9997) is better fitting than the pseudo-first-order (ZC11, R^2 = 0.8931) for the AG1 dye separation over ZrO_2/CeO_2 nano-adsorbent. The AG1 dye separation using the ZCP11 obeys the pseudo-first-order model and the value of the estimated adsorption capacity (cal. 24 mg/g) is in a good compact with the extracted data from the experimental (22.5 mg/g). But, the elimination of AG1 dye over the ZC11 sample follows the pseudo-second-order model and the calculated adsorption capacity value (cal. 33.1 mg/g) is in good agreement with the experimental one (32.8 mg/g). Besides, the power function model was applied to the experimental data for the elimination of the AG1 dye over ZrO_2/CeO_2 nano-adsorbent for the indication of the initial rate (W) and rate of the adsorption process (U). According to the R^2 values, the power function model fits well for the elimination of the dye using the ZCP11 and ZC11 samples as manifested in Fig. 8(d-f). The calculated initial rate and rate of the adsorption process from the power function model are shown in Table 2. The data shows that the initial rate of the AG1 dye adsorption using the synthesized ZC11 sample is faster than the fabricated ZCP11 sample. It clarifies that the adsorption process took a short time in the case of the ZC11 sample (90 min) than the ZCP11 sample (200 min) until the equilibrium stage has happened.

Table 2
Kinetic parameters for adsorption of AG1 dye using ZrO_2/CeO_2 adsorbent (ZCP11 and ZC11 samples).

model	Parameter	Values ZCP11	ZC11
Pseudo first order	$K_1(min^{-1})$	0.01257	0.03815
	$q_{m\ (cal)}$ (mg/g)	24	13.85
	R^2	0.935	0.8931
	$q_{m\ (exp)}$ (mg/g)	22.5	32.8
Pseudo second order	K_2(g/mg.min)	0.000251	0.00785
	$q_{m\ (cal)}$ (mg/g)	31.6	33.1
	R^2	0.8529	0.9997
	$q_{m\ (exp)}$ (mg/g)	22.6	32.8
Power function	W	1.044	19.58
	U	0.57324	0.112
	R^2	0.9648	0.9592
Intraparticle diffusion	K_I (mg/g $min^{0.5}$)	1.748	1.0528
	C (mg/g)	2.56	22.66
	R^2	0.9692	0.9011
	K_E	0.00215	0.002795
Outer diffusion	X_o	91.72	46.74
	R^2	0.9861	0.833
	K_o	0.00608	0.000216
pore diffusion	A	0.17612	0.65283
	R^2	0.9664	0.9576
liquid-film diffusion	K_E	0.0129	0.0305
	R^2	0.9201	0.9723

3.9. Adsorption mechanism

The AG1 dye adsorption using the synthesized nanocomposite (ZCP11 and ZC11 samples) can be studied using the following equations: intraparticle diffusion model (Eq. No. 11: plot q_t versus $t^{0.5}$) [5,8], liquid-film diffusion model (Eq. No 12: Boyd model; -ln(G) against t) [65,66], outer and external diffusion model (Eq. No. 13: Spahn and Schlunder model; lnX_t against t) [67-69] and pore diffusion model (Eq. No. 14: Bangham's equation: log R against log t) [70] as outlined in equations No. 11–14, respectively. These relations used to give data about the adsorbate amount and the rate of dye removal over the prepared samples as displayed in Fig. 9(a-d). The kinetic parameters determined from the various models and the collected data outlined in Table 2.

$$q_t = K_I t^{0.5} + C \quad (11)$$

$$\ln G = -K_L t \quad (12)$$

$$\ln X_t = \ln X_o - K_E t \quad (13)$$

$$\log R = \log(K_o/P) + \alpha \log t \quad (14)$$

Where, q_e and q_t are the amounts of dye adsorbed (mg/g) at equilibrium and time t (min), respectively, t (min) is contact time, k_I is the intraparticle diffusion constant (mg/g.$min^{0.5}$), and C is constant that gives an idea about the thickness of boundary layer (mg/g). The values of G calculated from the relation: G = [1-(q_t/q_e)] and K_L is liquid film

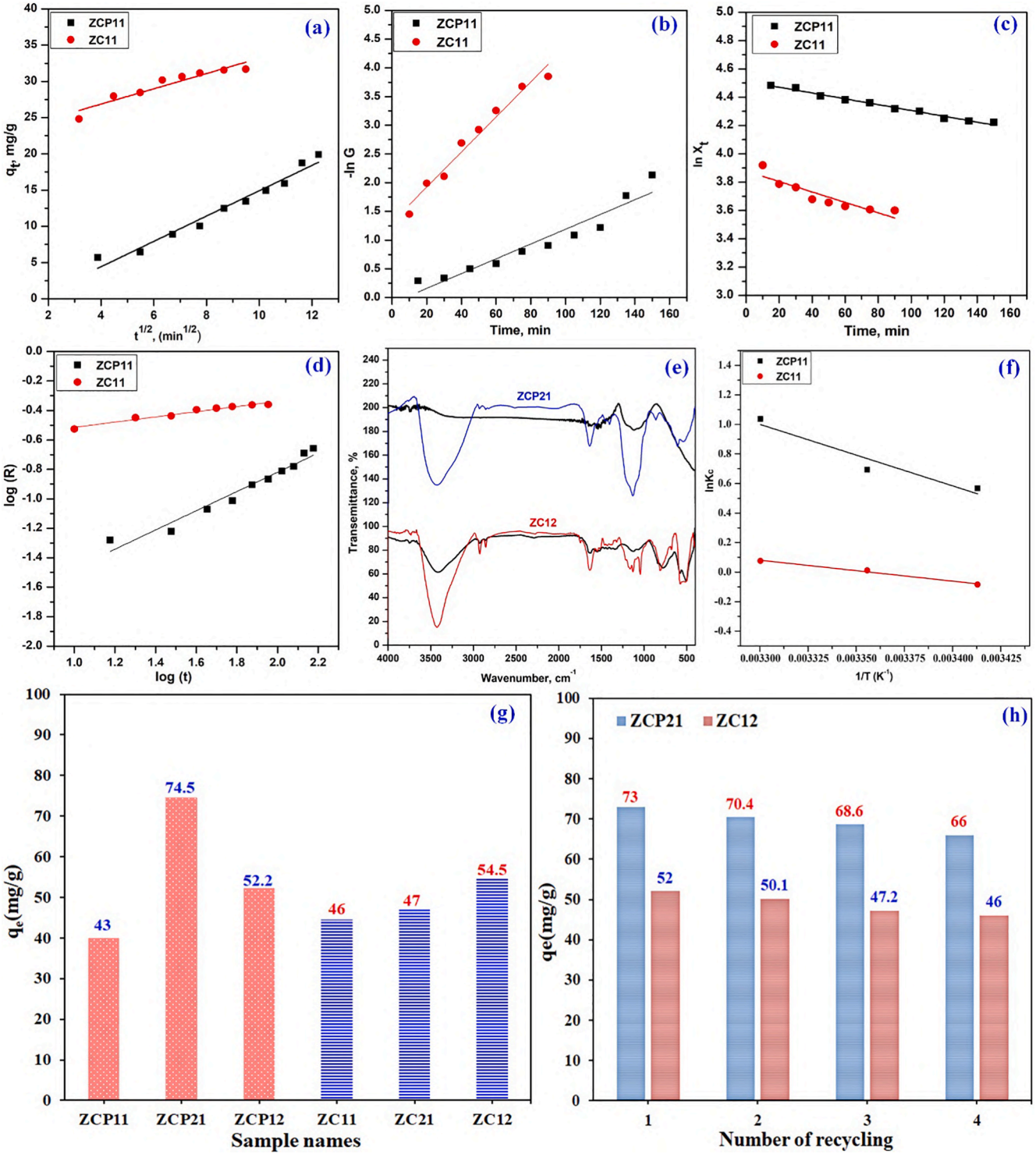

Fig. 9. Intraparticle diffusion model (a), liquid-film diffusion model (b), external diffusion model (c), pore diffusion model (d), FTIR spectra of ZC12 and ZCP21 before (black line) and after adsorption (red and blue lines) (e), Van't Hoff relation (f), the calculated qe at the applied optimum (g) and recycling the selected samples for the AG1 dye removal using ZrO_2/CeO_2 nanocomposites (h).

diffusion rate constant; min^{-1}. X_o is the initial dye concentration (mg/L), X_e is the equilibrium dye concentration (mg/L) and K_E is the external diffusion rate constant (min^{-1}). α (mg/g.min) and K_o (g/mg.min) are Bngham constants. R values determined from the relation: $R = \log[X_o/(X_o\text{-}q_e\ m)]$ and the P value calculated from the relation ($P = 2.303\ V/m$). m is the mass of the adsorbent in gram/litre and V is the volume of dye solution in mL.

Fig. 9(a) manifests the intraparticle diffusion model of the AG1 dye separation using the prepared ZCP11 and ZC11 samples. The extracted parameter values from linear relation are summarized in Table 2. According to the plot, the line does not pass the origin, and it is reflected that this model is not the only one for the illustration mechanism of the AG1 dye removal on ZrO_2/CeO_2 adsorbents (ZCP11 and ZC11 samples). But the determined R^2 values for ZCP11 and ZC11 samples showed the utility of the intraparticle diffusion model with the other models in the adsorption process. Additionally, the dye adsorption can be controlled

by other mechanisms: liquid film diffusion, outer diffusion, and pore diffusion.

Besides, It is clear that the linear plot of the liquid-film diffusion model (-ln(G) against t) are not passing through the origin and it is not only the rate-controlling step as manifested in Fig. 9(b). For R^2 values, It indicates that the liquid film diffusion model can be used for the interpretation mechanism of the AG1 dye adsorption using the synthesized ZrO_2/CeO_2 nano-adsorbent with the other models. Fig. 9(c) manifested the outer and external diffusion model (Eq. No. 11; lnX_t against t). The K_E and X_o values were founded to be 0.00215 min^{-1}, 0.002795 min^{-1}, 91.72 mg/L and 46.74 mg/L for ZCP11 and ZC11 samples, respectively. It appeared that the extracted information was close to the experimental concentration (100 mg/L) indicating the validity of this model for the ZCP11 sample and the inaccuracy for the ZC11 sample as displayed in Table 2. According to the R^2 values, the outer diffusion model can be explained the AG1 dye adsorption using the ZCP11 sample and it does not apply to the explanation of the adsorption over the ZC11 sample. Furthermore, the plot of log (R) with log (t) was pointed to be a direct linear with an excellent relationship coefficient (R^2 = 0.9664 and 0.9576) as displayed in Fig. 9(d). it pointed out that the rate-determining stage can be governed by the pore diffusion mechanism.

According to the extracted information, the AG1 dye adsorption using the synthesized ZCP11 sample can explain using more than one models according to R^2 values like the following: outer diffusion and liquid-film diffusion models can use for the transfer of dye from the solution to the surface following by the transfer the AG1 dye to the prepared ZrO_2/CeO_2 nanocomposites surface using the interparticle diffusion and pore diffusion models. On the other hand, the AG1 dye adsorption using the fabricated ZC11 sample is similar to the ZCP11 sample and it concluded as the following: liquid-film diffusion model can utilize for the transfer of the dye from the solution to the surface following by the transfer of the AG1 dye to the surface of the prepared ZrO_2/CeO_2 nanocomposites utilizing the interparticle diffusion and pore diffusion models.

Fig. 9(e) shows the FTIR spectrum for the ZCP21 and ZC12 samples after and before the AG1 dye adsorption. According to the obtained FTIR data of the AG1 dye adsorption using the synthesized samples, the bands of AG1 dye appeared plus the peaks of the zirconium and cerium oxide nanocomposites. The stretching vibrations of S-O of the sulphonic group appeared at 1050 cm^{-1} (shoulder at 1020 cm^{-1}) and 1120–1150 cm^{-1}. The bands between 1500 cm^{-1} and 1600 cm^{-1} referred to the aromatic rings of naphthalene and the stretching vibration of –C–N=O group. After the elimination process, the peak between 500 and 600 cm^{-1} is linked to the stretching vibration of Fe-O. According to the extracted information, the spectra manifested that the AG1 dye adsorbed over the synthesized ZrO_2/CeO_2 nanocomposite samples [71].

3.10. Thermodynamic studies

The temperature effect on the AG1 dye removal using the ZCP11 and ZC11 nano-adsorbents was investigated ranging from 293 K to 303 K. The thermodynamic parameters ΔH^o, ΔS^o and ΔG^o were examined utilizing Van't Hoff relation [5,72], (Equation No.15) as manifested in Fig. 9(f). The Gibbs free energy values (ΔG^o) for the AG1 dye adsorption using the prepared ZCP11 and ZC11 nano-adsorbents calculated from equation No. 16.

$$\ln K_c = \frac{H}{T} + A \quad (15)$$

$$\Delta G^\circ = \Delta H^\circ - T\Delta S^\circ \quad (16)$$

Where ΔH^o is enthalpy change, ΔS^o is entropy change, the k_c values were estimated from q_e/X_e and called the equilibrium constant (L/g), T is the temperature in Kevin (k) and R is the gas constant (8.314 J/ mol).

The plot of ($\ln k_c$) against (1/T) shows a straight line as illustrated in Fig. 7(f) with slope (H = -ΔH^o/R) and intercept (A = ΔS^o/R). Experimental parameters are summarized in Table 3. The elimination of AG1 dye using the fabricated ZCP11 and ZC11 nano-adsorbents was an endothermic process because of the positive value of ΔH^o. The ΔH^o values (cal. 29.46 and 11.8 KJ/mol for ZCP11 and ZC11 samples, respectively) are lower than 40 KJ/mol, therefore the elimination of AG1 dye using the ZCP11 and ZC11 samples is a physisorption process [3,73]. The positive charge of ΔS^o associated with the raise in the freedom degree of solution for the AG1 dye removal. The spontaneous dye removal was appeared according to the negative values of ΔG^o. Also, the AG1 dye removal using the fabricated ZCP11 and ZC11 samples is more favorable at high temperatures because the ΔG^o values reduced with the increasing temperature.

3.11. Effect of the obtained nanocomposites on the removal of AG1 dye

The obtained ZrO_2/ CeO_2 nanocomposites from the co-precipitation and combustion methods (ZCP11, ZCP21, ZCP12, ZC11, ZC21 and ZC12 samples) were studied at the optimum conditions: pH = 3, 250 mg/L, 0.05 g dose adsorbents, and equilibrium time (200 min for ZCP11, ZCP21 and ZCP12 samples), (90 min for ZC11, ZC21 and ZC12 samples). The removal capacities of ZrO_2/CeO_2 nanocomposites are determined and represented in Fig. 9(g).

3.12. Comparison of adsorption capacities of the synthesized ZrO_2/CeO_2 nanocomposites with different adsorbents for the removal of AG1 dye

The adsorption capacities of ZrO_2/CeO_2 adsorbents for the elimination of AG1 dye compared with the adsorbents in the literature [3,6,50,51,71,74-78]. The obtained information appeared that the fabricated ZrO_2/CeO_2 nanocomposites can be used as adsorbents for the elimination of AG1 dye according to the determined adsorption capacity as summarized in Table 4.

3.13. Recycling and regeneration of the synthesized ZrO_2/CeO_2 nano-adsorbents

The capability of regeneration of the prepared ZrO_2/ CeO_2 adsorbents (ZCP21 and ZC12 samples) was investigated under the optimum conditions. The dyes were eluted by various eluents including ethanol, methanol, HCl/NaOH solution following by calcination at 300 °C for 10 min. After four cycles, the fabricated ZrO_2/ CeO_2 adsorbents can be reused for the elimination of AG1 dye several times with high capacity as illustrated in Fig. 9(h). The extracted information confirms that the recycling of the fabricated ZrO_2/CeO_2 nanocomposites (ZCP21 and ZC12 samples) can be accepted as adsorbents for cleaning the solution from AG1 dye under acceptable conditions.

4. Conclusions

ZrO_2/CeO_2 nano-adsorbents synthesized utilizing co-precipitation and hybrid combustion-ultrasonication methods. The fabricated ZrO_2/ CeO_2 nanocomposites were examined using different tools for the study

Table 3
Thermodynamic parameters for the AG1 dye adsorption using ZrO_2 /CeO_2 adsorbents (ZCP11 and ZC11 samples).

Adsorbent	Temperature, (°K)	ln K_c	ΔG° (KJ/ mol)	ΔH° (KJ/ mol)	ΔS° (KJ/ mol)
ZCP11	293	0.5672	−1.3165	29.46	0.105
	298	0.6888	−1.8416		
	303	0.9672	−2.3667		
ZC11	293	−0.0842	0.1934	11.796	0.0396
	298	0.0116	−0.0046		
	303	0.0755	−0.2026		

Table 4
Comparison of Adsorption capacities of the synthesized ZrO_2 /CeO_2 adsorbents with various adsorbents.

Adsorbents	q, (mg/g)	Refs
Industrial sludge	10	3
Halloysite-iron oxide nanocomposite	11.2	6
Tafla	23.86	50
Kaolinite	25.8	50
Charcoal	232.56	50
TAC based activated carbon	545	51
Mg/Al layered double oxides	193.4	71
Multifunctional silica (SiO_2@Nap)	79	74
Treated red mud	12.7	75
Acid activated Bentonite	253.14	76
Pistachio-nut shell activated carbon (PAC)	63.4	77
ZnS:Cu nanoparticles	38.6	77
ZnS:Cu nanoparticles/PAC	76.0	77
MPM–PEHA nanocomposite	1583	78
ZCP11	43	This study
ZCP12	52.2	This study
ZCP21	74.5	This study
ZC11	46	This study
ZC12	54.5	This study
ZC21	47	This study

of the structure and morphology. The ZrO_2/CeO_2 nanocomposites were used as adsorbents for the elimination of Acid Green 1 from the aqueous phase utilizing the batch technique. The elimination process of the AG1 dye using the prepared nanocomposites (ZCP11, ZCP21, ZCP12, ZC11, ZC21 and ZC12 samples) was examined using different adsorption parameters: pH = 3, 250 mg/L of AG1 dye, 0.05 g dose adsorbents, and equilibrium time (200 min for ZCP11, ZCP21 and ZCP12 samples), (90 min for ZC11, ZC21 and ZC12 samples). The removal capacities are estimated to be in the range of 43–74.5 and 46–54.5 mg/g for the ZrO_2/CeO_2 nanocomposites using coprecipitation and hybrid combustion-ultrasonication methods, respectively. The extracted information was fitted well with Langmuir adsorption isotherm and followed pseudo-first-order for ZCP11 sample and pseudo-second-order for ZC11 sample. Also, the elimination of Acid Green 1 on ZCP11 and ZC11 nano-adsorbents was spontaneous, physisorption and endothermic process. Finally, ZrO_2/CeO_2 nanocomposites can be used as very effectively and economically nano-adsorbents for the elimination of AG1 from aqueous media.

CRediT authorship contribution statement

Ayman A. Ali: Methodology, Conceptualization, Data curation, Formal analysis, Investigation, Resources, Validation, Visualization, Writing - original draft, Writing - review & editing. **Sayed A. Shama:** Conceptualization, Visualization, Supervision, original draft preparation -review & editing. **Alaa S. Amin:** Conceptualization, Visualization, Supervision, Writing - review & editing. **Sahar R. EL-Sayed:** Methodology, Data curation, Formal analysis, Resources, Writing - original draft.

Declaration of Competing Interest

The authors declare that they have no known competing financial interests or personal relationships that could have appeared to influence the work reported in this paper.

Acknowledgements

The authors express their thanks to Benha University, Egypt for support of the current research.

References

[1] A. Kausar, M. Iqbal, A. Javed, K. Aftab, H.N. Bhatti, S. Nouren, J. Mol. Liq. 256 (2018) 395–407.
[2] L. Bartoňová, L. Ruppenthalová, M. Ritz, Chin. J. Chem. Eng. 25 (2017) 37–44.
[3] M.F. Attallah, I.M. Ahmed, M.M. Hamed, Environ. Sci. Pollut. Res. 20 (2013) 1106–1116.
[4] F. Dehghani, S. Hashemian, A. Shibani, J. Ind. Eng. Chem. 48 (2017) 36–42.
[5] A.A. Ali, E.M. Elfiky, I.S. Ahmed, A.A. Khalil, T.Y. Mohamed, Desalin. Water Treat. 193 (2020) 83–94.
[6] R. Riahi-Madvaar, M.A. Taher, H. Fazelirad, Appl. Clay Sci. 137 (2017) 101–106.
[7] M. Gabal, F. Al-Solami, Y. Al Angari, A. Ali, A. Al-Juaid, K.-W. Huang, M. Alsabban, Ceram. Int. 45 (2019) 16530–16539.
[8] A.A. Ali, I.S. Ahmed, E.M. Elfiky, J. Inorg. Organomet. Polym. 31 (2021) 384–396.
[9] A.A. Ali, I.S. Ahmed, Mater. Chem. Phys. 238 (2019) (1903) 121888–121903.
[10] A.A. Ali, E. El Fadaly, I.S. Ahmed, Dyes Pigm. 158 (2018) 451–462.
[11] G. Wang, Q. Mu, T. Chen, Y. Wang, J. Alloys Compd. 493 (2010) 202–207.
[12] S. Hassanzadeh-Tabrizi, M. Mazaheri, M. Aminzare, S. Sadrnezhaad, J. Alloys Compd. 491 (2010) 499–502.
[13] S. Manikandan, A.A. Irudayaraj, A.D. Raj, M. Kirubanithy, Mater. Today: Proc. 2 (2015) 4378–4383.
[14] S. Supakanapitak, V. Boonamnuayvitaya, S. Jarudilokkul, Mater. Charact. 67 (2012) 83–92.
[15] A. Bumajdad, J. Eastoe, A. Mathew, Adv. Colloid Interface Sci. 147–148 (2009) 56–66.
[16] A.A. Ali, S.R. El-Sayed, S.A. Shama, T.Y. Mohamed, A.S. Amin, Desalin. Water Treat. 204 (2020) 124–135.
[17] B. Sathyaseelan, E. Manikandan, I. Baskaran, K. Senthilnathan, K. Sivakumar, M. Moodley, R. Ladchumananandasivam, M. Maaza, J. Alloys Compd. 694 (2017) 556–559.
[18] M.N. Tahir, L. Gorgishvili, J. Li, T. Gorelik, U. Kolb, L. Nasdala, W. Tremel, Solid State Sci. 9 (2007) 1105–1109.
[19] H. Cui, Q. Li, S. Gao, J.K. Shang, J. Ind. Eng. Chem. 18 (2012) 1418–1427.
[20] L. Li, W. Wang, Solid State Commun. 127 (2003) 639–643.
[21] M. Verma, V. Kumar, A. Katoch, Mater. Chem. Phys. 212 (2018) 268–273.
[22] A. Bhowmick, P. Jana, N. Pramanik, T. Mitra, S.L. Banerjee, A. Gnanamani, M. Das, P.P. Kundu, Carbohydr. Polym. 151 (2016) 879–888.
[23] F. Wang, K. Pan, S. Wei, Y. Ren, H. Zhu, H.-H. Wu, Q. Zhang, Ceram. Int. (2020).
[24] B. Anjaneyulu, G. Nagamalleswara Rao, K. Prahlada Rao, Materials Today: Proceedings (2020).
[25] C.d. Santos, I.F. Coutinho, J.E.V. Amarante, M.F.R.P. Alves, M.M. Coutinho, C.R. Moreira da Silva, J. Mech. Behav. Biomed. Mater. 116 (2021) 104372.
[26] S.A. Singh, B. Vemparala, G. Madras, J. Environ. Chem. Eng. 3 (2015) 2684–2696.
[27] J. Lin, S. He, X. Wang, H. Zhang, Y. Zhan, Colloids Surf., A 561 (2019) 301–314.
[28] T. Zhu, T. Zhu, J. Gao, L. Zhang, W. Zhang, J. Fluorine Chem. 194 (2017) 80–88.
[29] K.R. Alhooshani, Arab. J. Chem. 12 (2019) 2585–2596.
[30] H. Pei, H. Zhang, Z. Mo, R. Guo, N. Liu, Q. Jia, Q. Gao, Ceram. Int. 46 (2020) 3827–3836.
[31] S. Hyok Ri, F. Bi, A. Guan, X. Zhang, J. Colloid Interface Sci. 586 (2021) 836–846.
[32] M. Vanitha, I.M. Joni, P. Camellia, N. Balasubramanian, Ceram. Int. 44 (2018) 19725–19734.
[33] R. Gao, D. Zhang, P. Maitarad, L. Shi, T. Rungrotmongkol, H. Li, J. Zhang, W. Cao, J. Phys. Chem. C 117 (2013) 10502–10511.
[34] M. Racik K, A. Manikandan, M. Mahendiran, J. Madhavan, M. Victor Antony Raj, M.G. Mohamed, T. Maiyalagan, Ceram. Int., 46 (2020) 6222–6233.
[35] I.S. Ahmed, S.A. Shama, M.M. Moustafa, H.A. Dessouki, A.A. Ali, Spectrochim. Acta, Part A 74 (2009) 665–672.
[36] L. Deng, S. He, S. Huang, J. Wang, D. He, S. He, Y. Luo, Procedia Eng. 102 (2015) 417–423.
[37] I.S. Ahmed, S.A. Shama, H.A. Dessouki, A.A. Ali, Spectrochim. Acta, Part A 81 (2011) 324–333.
[38] M.A. Gabal, F. Al-Solami, Y.M. Al Angari, A. Awad, A.A. Al-Juaid, A. Saeed, J. Mater. Sci. - Mater. Electron. 31 (2020) 3146–3158.
[39] L. Armelao, D. Barreca, G. Bottaro, A. Gasparotto, E. Tondello, M. Ferroni, S. Polizzi, Chem. Vap. Deposition 10 (2004) 257–264.
[40] H. Pouretedal, Z. Tofangsazi, M. Keshavarz, J. Alloys Compd. 513 (2012) 359–364.
[41] M.Y. Nassar, A.A. Ali, A.S. Amin, RSC Adv. 7 (2017) 30411–30421.
[42] R. Razzaq, H. Zhu, L. Jiang, U. Muhammad, C. Li, S. Zhang, Ind. Eng. Chem. Res. 52 (2013) 2247–2256.
[43] W. Wang, K. Wu, P. Liu, L. Li, Y. Yang, Y. Wang, Ind. Eng. Chem. Res. 55 (2016) 7598–7603.
[44] Q. Wang, A. Tang, L. Zhong, X. Wen, P. Yan, J. Wang, Powder Technol. 339 (2018) 872–881.
[45] M. Bhowmik, M. Kanmani, A. Debnath, B. Saha, Powder Technol. 354 (2019) 496–504.
[46] P. Scherrer, Phys 2 (1918) 98–100.
[47] X. Gan, Z. Yu, K. Yuan, C. Xu, X. Wang, L. Zhu, G. Zhang, D. Xu, Ceram. Int. 43 (2017) 14183–14191.
[48] S. Usharani, V. Rajendran, Chin. J. Phys 55 (2017) 2588–2596.
[49] E.A. Abdelrahman, R. Hegazey, J Composites Part B: Engineering 166 (2019) 382–400.
[50] S. Rizk, M.M. Hamed, Desalin. Water Treat. 56 (2015) 1536–1546.
[51] W. Dai, H. Yu, N. Ma, X. Yan, Korean J. Chem. Eng. 32 (2015) 335–341.
[52] S.-C. Tsai, K.-W. Juang, J. Radioanal. Nucl. Chem. 243 (2000) 741–746.
[53] W. Yu, K. Sepehrnoori, T.W. Patzek, SPE J. 21 (2016) 589–600.
[54] K.K. Choy, J.F. Porter, G. McKay, J. Chem. Eng. Data 45 (2000) 575–584.

[55] G.P. Jeppu, T.P. Clement, J. Contam. Hydrol. 129 (2012) 46–53.
[56] B.E. Reed, M.R. Matsumoto, Sep. Sci. Technol. 28 (1993) 2179–2195.
[57] K. Vijayaraghavan, T. Padmesh, K. Palanivelu, M. Velan, J. Hazard. Mater. 133 (2006) 304–308.
[58] X.-S. Wang, Y. Qin, Process Biochem. 40 (2005) 677–680.
[59] S.V. Mohan, J. Karthikeyan, Environ. Pollut. 97 (1997) 183–187.
[60] E.W. Shin, K. Karthikeyan, M.A. Tshabalala, Bioresour. Technol. 98 (2007) 588–594.
[61] Y. Bulut, Z. Tez, J. Hazard. Mater. 149 (2007) 35–41.
[62] L. Xiong, C. Chen, Q. Chen, J. Ni, J. Hazard. Mater. 189 (2011) 741–748.
[63] G. Akkaya, A. Özer, Process Biochem. 40 (2005) 3559–3568.
[64] V. Srihari, A. Das, Desalin. 225 (2008) 220–234.
[65] D. D. M. R. E. A, W. W. M. K. E. H, I. S. S, P. N, I. M. C. M, RSC Adv., 6 (2016) 98682-98692.
[66] G.E. Boyd, A.W. Adamson, L.S. Myers Jr., J. Am. Chem. Soc. 69 (1947) 2836–2848.
[67] Y. Wu, M. Zhang, H. Zhao, S. Yang, A. Arkin, RSC Adv. 4 (2014) 61256–61267.
[68] H. Spahn, E.U. Schlünder, Chem. Eng. Sci. 30 (1975) 529–537.
[69] E.A. Abdelrahman, J. Mol. Liq. 253 (2018) 72–82.
[70] V.S. Mane, I. Deo Mall, V. Chandra Srivastava, J. Environ. Manage. 84 (2007) 390–400.
[71] F. Zhang, Z. Ni, S. Xia, X. Liu, Q. Wang, Chin. J. Chem. 27 (2009) 1767–1772.
[72] J.V. Milojković, M.L. Mihajlović, M.D. Stojanović, Z.R. Lopičić, M.S. Petrović, T. D. Šoštarić, M.Đ. Ristić, J. Chem. Technol. Biotechnol. 89 (2014) 662–670.
[73] E.A. Abdelrahman, R.M. Hegazey, R.E. El-Azabawy, J. Mater. Res. Technol. 8 (2019) 5301–5313.
[74] S. Chatterjee, H. Gohil, A.R. Paital, ChemistrySelect 2 (2017) 5348–5359.
[75] G.K. Mohan, A.N. Babu, K. Kalpana, K. Ravindhranath, Der Pharma Chemica 8 (2016) 403–414.
[76] L. Jayalakshmi, V. Devadoss, K. Ananthakumar, G. Kanthimathi, Int. Res. J. Environ. Sci. 3 (2014) 21–26.
[77] N. Masoudian, M. Rajabi, M. Ghaedi, A. Asghari, Appl. Organomet. Chem. 32 (2018), e4369.
[78] A. Pourjavadi, A. Abedin-Moghanaki, S.A. Nasseri, RSC Adv. 6 (2016) 7982–7989.